

# Multidimensional Vascularized Polymers using Degradable Sacrificial Templates

Ryan C. R. Gergely, Stephen J. Pety, Brett P. Krull, Jason F. Patrick, Thu Q. Doan, Anthony M. Coppola, Piyush R. Thakre, Nancy R. Sottos, Jeffrey S. Moore, and Scott R. White\*

Complex multidimensional vascular polymers are created, enabled by sacrificial template materials of 0D to 3D. Sacrificial material consisting of the commodity biopolymer poly(lactic acid) is treated with a tin catalyst to accelerate thermal depolymerization, and formed into sacrificial templates across multiple dimensions and spanning several orders of magnitude in scale: spheres (0D), fibers (1D), sheets (2D), and 3D printed. Templates are embedded in a thermosetting polymer and removed using a thermal treatment process, vaporization of sacrificial components (VaSC), leaving behind an inverse replica. The effectiveness of VaSC is verified both *ex situ* and *in situ*, and the resulting structures are validated via flow rate testing. The VaSC platform is expanded to create vascular and porous architectures across a wide range of size and geometry, allowing engineering applications to take advantage of vascular designs optimized by biology.

and autonomous materials.<sup>[22–24]</sup> Porous materials not only mediate transport of fluids in filtration,<sup>[25]</sup> but also regulate ion exchange in battery electrodes<sup>[26]</sup> and separator films,<sup>[27]</sup> facilitate new tissue growth in bioscaffolds,<sup>[28–31]</sup> and increase strength-to-weight ratio in structural solids.<sup>[32]</sup> No fabrication technique has emerged with the flexibility to control size and dimensionality across all of these applications.

Esser-Kahn et al.<sup>[23]</sup> recently introduced the vaporization of sacrificial components (VaSC) technique. In their work, 1D poly(lactic acid) (PLA) fibers are treated with tin(II) oxalate (SnOx) catalyst to undergo thermal depolymerization and vaporization at  $\approx 200$  °C. After

embedding “sacrificial” PLA in a thermoset composite and subsequent thermal treatment, the fibers vaporized, forming vasculature that is their inverse replica. By introducing various functional fluids into the microvasculature, desirable properties were imparted on the composite, such as thermal regulation, magnetic or electrical modulation, and *in situ* reaction of chemical species.<sup>[23]</sup> In this work, we extend the application of VaSC by introducing sacrificial templates across all levels of spatial dimensionality and spanning several orders of magnitude in size, enabling a wide range of vascular and porous architectures.

## 1. Introduction

Biological systems employ complex, composite architectures that enable homeostatic functionality. A common necessity underlying many of these systems is the transport of fluids that distribute nutrients, remove waste, and provide thermal regulation.<sup>[1]</sup> Parallels exist in engineered materials, however the architectures are comparatively less complex. Channels for mass and heat transport are used in micro-/nanofluidics,<sup>[2–10]</sup> microelectromechanical systems,<sup>[10–15]</sup> gas capture,<sup>[16,17]</sup> flow batteries,<sup>[18]</sup> fuel cells,<sup>[19]</sup> heat exchangers,<sup>[20,21]</sup>

R. C. R. Gergely  
Department of Mechanical Science and Engineering  
Beckman Institute for Advanced Science and Technology  
University of Illinois at Urbana-Champaign  
Urbana, IL 61801, USA

S. J. Pety, B. P. Krull, T. Q. Doan, Prof. N. R. Sottos  
Department of Materials Science and Engineering  
Beckman Institute for Advanced Science and Technology  
University of Illinois at Urbana-Champaign  
Urbana, IL 61801, USA

Dr. J. F. Patrick  
Department of Civil and Environmental Engineering  
Beckman Institute for Advanced Science and Technology  
University of Illinois at Urbana-Champaign  
Urbana, IL 61801, USA

A. M. Coppola, Prof. S. R. White  
Aerospace Engineering  
Beckman Institute for  
Advanced Science and Technology  
University of Illinois at Urbana-Champaign  
Urbana, IL 61801, USA  
E-mail: swhite@illinois.edu

Dr. P. R. Thakre  
Beckman Institute for Advanced Science and Technology  
University of Illinois at Urbana-Champaign  
Urbana, IL 61801, USA

Prof. J. S. Moore  
Department of Chemistry  
Beckman Institute for Advanced Science and Technology  
University of Illinois at Urbana-Champaign  
Urbana, IL 61801, USA



DOI: 10.1002/adfm.201403670

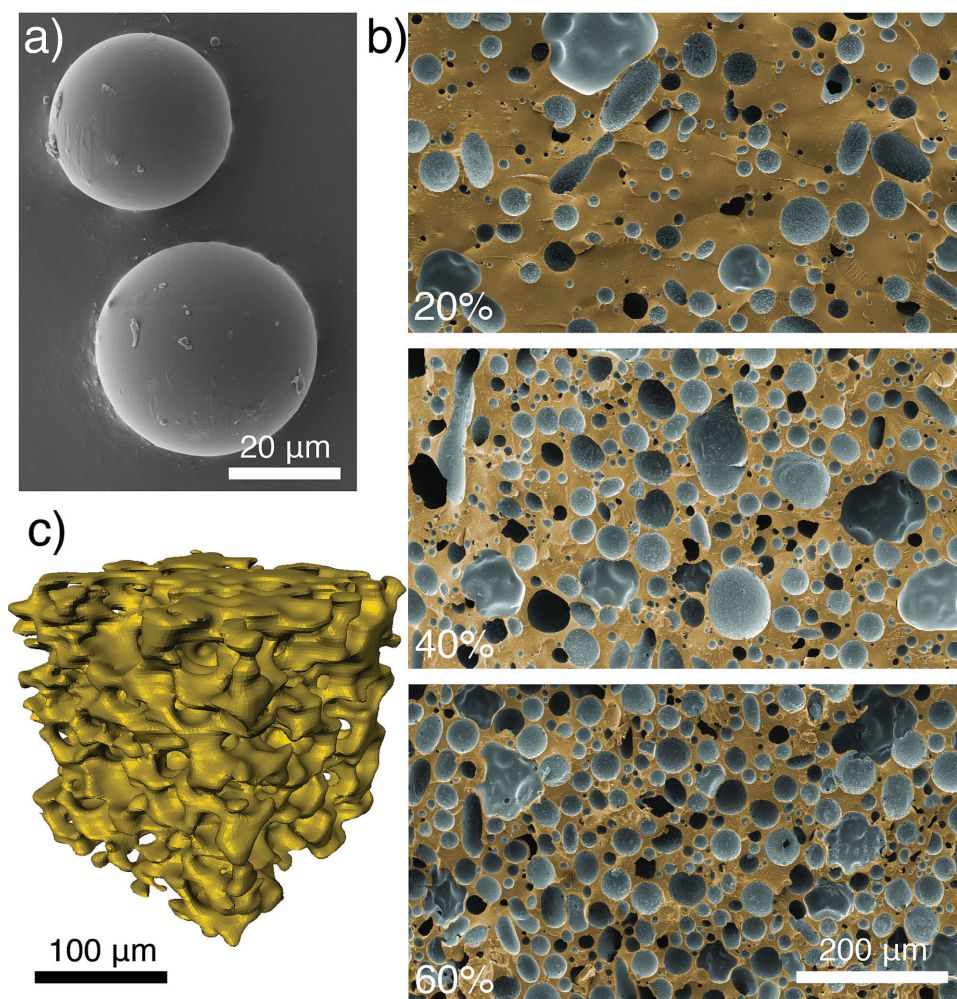


**Figure 1.** 0D sacrificial template and inverse architectures created after VaSC: a) individual microspheres (scanning electron microscopy (SEM) images); b) cross sections of closed-cell porous epoxy created after VaSC using sacrificial microspheres mixed at 20, 40, and 60 wt% (SEM, gold color overlay indicating nonporous area); and c) 3D X-ray computed microtomographic (microCT) reconstruction of open-cell porous epoxy (56 vol% porosity) after VaSC of sintered sacrificial microspheres.

Several fabrication techniques to directly form complex vascular architectures exist, including electrostatic discharge,<sup>[33]</sup> 3D printing,<sup>[29,30]</sup> and lamination of 2D structures.<sup>[2,3,17,20]</sup> Alternatively, a sacrificial template in the shape of the desired vascular architecture can be integrated into the host material, and later removed through melting,<sup>[22,34]</sup> dissolution,<sup>[4–6,30,35]</sup> chemical etching,<sup>[21,26]</sup> or thermal vaporization.<sup>[7–16,23,24,36]</sup> Templates prevent infiltration or collapse of cavities during fabrication, and eliminate the necessity for registration of 2D layers in lamination techniques. Among existing sacrificial fabrication techniques, VaSC provides additional advantages. Thermal depolymerization occurs simultaneously throughout the sacrificial material, expediting the removal of large structures. In contrast, etching or dissolution occurs just at the exposed surfaces. Depolymerization also results in a gaseous byproduct, facilitating the evacuation of high aspect ratio microchannels due to both the pressurized expansion of the gas and its low viscosity, typically  $\approx 3$  orders of magnitude less than a liquid. In addition, gaseous products may also diffuse through surrounding material to allow removal of fully enclosed sacrificial

templates.<sup>[7,10–13]</sup> Previous reports of thermally degradable polymers require complicated syntheses or exhibit high decomposition temperatures that would damage a surrounding polymer matrix.<sup>[7–15]</sup> VaSC overcomes these limitations by using a commodity thermoplastic biopolymer (PLA), doped with tin catalyst to reduce the depolymerization temperature of the template material below the decomposition temperature of the surrounding matrix.<sup>[23]</sup> This vascularization process is accomplished without reduction in mechanical performance of the host material.<sup>[23,24,37]</sup>

## 2. Results and Discussion

### 2.1. Dimensionality

Sacrificial templates with dimensionality ranging from 0D to 3D enable the creation of complex vascular and porous architectures in thermosetting polymers. Sacrificial microspheres (0D, **Figure 1a**) are used to form both closed and open

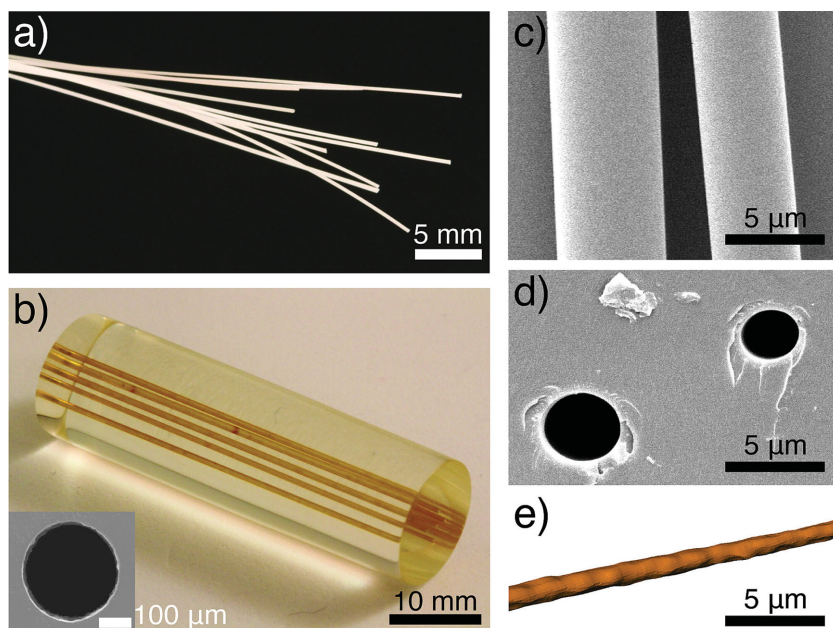


**Figure 2.** 1D sacrificial templates and inverse architectures created after VaSC: a) melt-spun sacrificial fibers  $\approx 300 \mu\text{m}$  diameter; b) parallel array of five microchannels in epoxy created from melt-spun sacrificial fibers, microchannel cross section (SEM, inset); c) electrospun sacrificial fibers  $\approx 5 \mu\text{m}$  diameter (SEM); and d, e) microchannels in epoxy created after VaSC from electrospun sacrificial fibers, d) cross sections (SEM), e) 3D reconstruction of microchannel filled with a fluorescent dye from confocal fluorescence microscope image stack.

(interconnected) cell porosity. Microspheres with polydisperse diameters averaging  $23 \mu\text{m}$  (Figure S1, Supporting Information) are produced via a solvent evaporation technique. PLA (4 wt% with respect to solvent) and liquid catalyst (tin(II) octoate, SnOc) are dissolved in a solvent (dichloromethane, DCM), then added to an aqueous surfactant mixture (1 wt% poly(vinyl alcohol), PVA) and mechanically stirred. Upon evaporation of the solvent, the catalyst is incorporated into solid sacrificial microspheres. Closed-cell porosity is created in a thermoset epoxy matrix by mixing sacrificial microspheres (containing 17 wt% SnOc) into the liquid epoxy resin (up to 60 wt%,  $\approx 56 \text{ vol}\%$ ) prior to solidification, with VaSC (thermal treatment for 24 h at  $200^\circ\text{C}$  under vacuum) revealing the porous structure, and increasing microsphere concentration resulting in higher porosity (Figure 1b, Table S2, Supporting Information). To create open-cell porosity, sacrificial microspheres (containing 5 wt% SnOc) are first sintered to form a porous scaffold of sacrificial material.<sup>[32]</sup> The sacrificial template is then vacuum infiltrated with epoxy resin, allowed to solidify, and postcured. After VaSC an interconnected porous structure is formed with  $\approx 56 \text{ vol}\%$  porosity, determined using X-ray computed microtomography (microCT) (Figure 1c, Video S1, Supporting Information).

Melt spinning and electrospinning were used to create 1D sacrificial fibers with diameters spanning three orders of magnitude (Figure 2). Melt-compounded precursor material (PLA, 5 wt% SnOx) is melt spun into sacrificial fibers (Figure 2a) and subsequently drawn to diameters  $\approx 300 \mu\text{m}$  to increase tensile strength and postyield ductility (Figure S2, Supporting Information). Sacrificial fibers embedded in epoxy produce channels with circular cross section as shown in the parallel array in Figure 2b. Sacrificial fibers of much smaller diameter

( $\approx 5 \mu\text{m}$ ) are produced via electrospinning (Figure 2c).<sup>[8,35,38]</sup> Tin catalyst is incorporated by adding liquid SnOc (5 wt% with respect to PLA) to the precursor solution for electrospinning (PLA, 25 wt% in 3:1 by volume chloroform/acetone). After embedding the electrospun sacrificial fibers in epoxy, and VaSC, hollow capillaries are produced (Figure 2d,e).

2D sacrificial templates are laser cut from  $\approx 550 \mu\text{m}$  thick sheets of melt-compounded sacrificial material (PLA, 5 wt% SnOx) produced via hot pressing. The 2D pattern can be freely designed in computer-aided drafting (CAD) software and cut by a computer-controlled  $\text{CO}_2$  laser. We created a branched planar network for microfluidic evaluation, which consists of two generations of bifurcations resulting in four flow pathways that stem from a single inlet and reconverge at the outlet (Figure 3). Channel widths reduce from 1 to 0.75 to 0.5 mm as the number of flow paths increase (Table S3, Supporting Information). The sacrificial template was embedded in epoxy and subjected to VaSC to produce the microchannel network.

3D printing was used to create a sacrificial vascular template in an additive fashion. Feedstock was made for a commercial fused-deposition modeler (FDM) out of melt-compounded sacrificial material (PLA, 5 wt% SnOx). A branching structure with a largest diameter of 10 mm and a smallest diameter of 1.5 mm (Figure S3a, Supporting Information) was designed using 3D CAD software (SolidWorks), and printed (Figure 4a,b). The sacrificial template was embedded in epoxy, and subjected to VaSC to reveal the tree-like vasculature (Figure 4c).

## 2.2. VaSC Characterization

Removal of sacrificial material occurs through thermal depolymerization of PLA and evaporation of lactide monomer. The

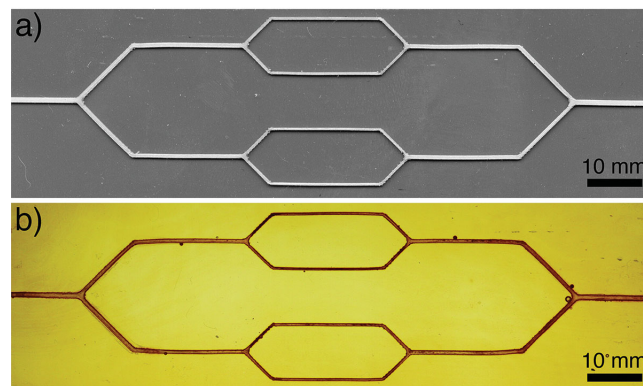


**Figure 3.** 2D sacrificial template and inverse architecture created after VaSC: a) laser cut template from sacrificial sheet; and b) bifurcating, planar network in epoxy created after VaSC using laser cut template.

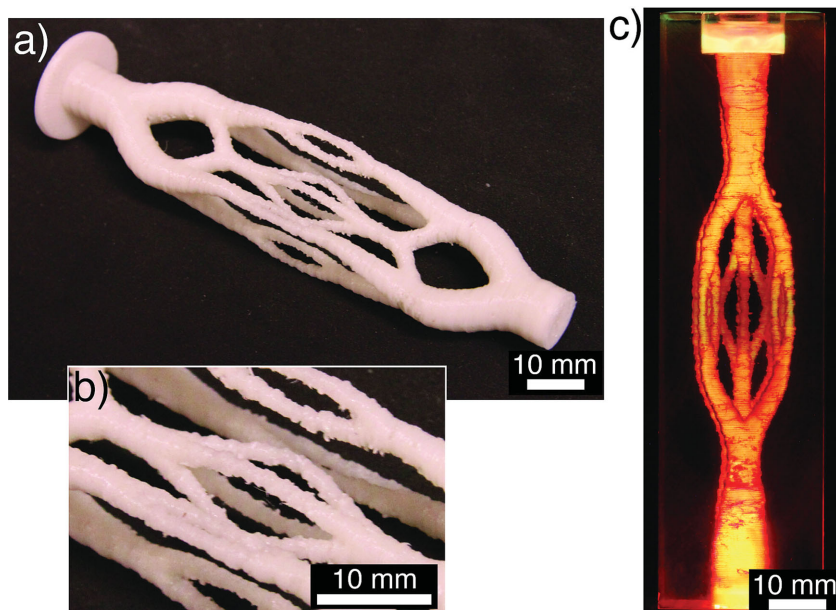


**Figure 4.** 3D sacrificial template and inverse architecture created after VaSC: a) printed tree-like sacrificial 3D structure, b) zoomed 2 $\times$ , showing print fidelity; and c) branched vasculature in epoxy after VaSC filled with chemiluminescent dye.

depolymerization temperature of neat PLA is  $\approx 280$  °C, but can be reduced by  $\approx 100$  °C with the addition of a tin catalyst.<sup>[23,36]</sup> Commercially spun PLA fibers can be treated by swelling with a solvent mixture containing trifluoroethanol and water to impregnate solid catalyst (SnOx) particles within the fiber.<sup>[23]</sup> To better disperse the tin catalyst, PLA and SnOx were melt compounded to fabricate sacrificial fibers, sheets, and 3D-printing filament. The improved homogeneity (Figure S4, Supporting Information) decreases the potential for incomplete clearing of cavities. Sacrificial microspheres and electrospun fibers, however, are similar in size to SnOx particles (up to  $\approx 50$   $\mu\text{m}$ ), thus an alternative liquid catalyst (SnOc)<sup>[36]</sup> was incorporated into these materials.

To evaluate the effectiveness of VaSC among the various templates, we employ two different experimental methods. First, ex situ vaporization is characterized using isothermal thermogravimetric analysis (iTGA) at 200 °C under continuous nitrogen purge (Figure 5a). Although catalyst type differs depending on the fabrication technique, all samples except solvent-impregnated commercial fibers contain 5 wt% of the appropriate catalyst (SnOx, SnOc) incorporated into PLA (Ingeo 4043D or Ecorene NW40). The catalyst incorporated using solvent impregnation is more difficult to control, with the concentration typically  $\approx 16\%$ . The residual mass in the TGA traces is indicative of the amount of catalyst incorporated. Specimens containing SnOx (solid particles) decompose in  $\approx 14$  h, while specimens containing SnOc (liquid) decompose in  $\approx 1$  h. Although PLA containing SnOc shows superior decomposition performance; it degrades so quickly at the processing temperatures for melt compounding, melt spinning, and hot pressing ( $\approx 175$  °C, Figure S5, Supporting Information), that it becomes impractical for these techniques. In contrast, the slower depolymerization rate with SnOx makes it well suited for

melt-processing techniques, demonstrating the tunability of VaSC for the intended processing method.

VaSC is also evaluated in situ by measuring the mass loss of template materials embedded in epoxy and subjected to 200 °C under vacuum. The four templates tested and their respective volume fractions in epoxy are: untreated commercial fibers ( $\approx 19$  vol%) (no catalyst, Nexttrusion GmbH), sacrificial melt-spun fibers ( $\approx 25$  vol%), sacrificial microspheres mixed at 60 wt% ( $\approx 56$  vol%), and sintered sacrificial microspheres ( $\approx 58$  vol%) (Figure 5b, Table 1). A separate set of specimens was placed in the vacuum oven for each exposure time, with the mass measured before and after the test used to determine the mass loss. The mass lost after the maximum in situ exposure time of 24 h for each specimen is within 10% of the expected value (the sacrificial material content). The initial content of sacrificial material is separately determined. For fiber specimens the mass per unit length of the fibers and the length of each specimen (containing three embedded fibers) was measured. These measurements

are used to estimate the mass of sacrificial material in each specimen. For the mixed sphere specimens (closed cell), the initial quantity of spheres is known to be 60 wt%. For sintered spheres embedded in epoxy (open cell), iTGA at 200 °C (Figure S7, Supporting Information) shows an average residual mass of 39%; thus, the sacrificial material content is taken to be 61%. The time required for complete in situ removal of sacrificial material, indicated by the plateau in mass, is longer than measured ex situ by iTGA. The most pronounced delay is for the specimens in which sacrificial microspheres were mixed into epoxy. This disparity is presumably due to the complete encapsulation of the sacrificial microspheres by epoxy with no direct pathway for monomer evaporation. Nevertheless, monomer gas diffuses through the polymer matrix leading to significant mass loss and producing hollow cavities after VaSC treatment (Figure 1b).

### 2.3. Flow Rate Testing

Vascular and porous architectures constructed from template materials of each level of dimensionality (0D–3D) were evaluated by flow rate testing using deionized water (0D–2D) or 85/15 wt% glycerol/water (3D). Experiments were performed at room temperature (RT) under laminar flow conditions (Table S4, Supporting Information) and compared to appropriate predictive models.

We tested rectangular specimens ( $15 \times 15 \times 1$  mm<sup>3</sup>) of the open-cell porous (0D) structure shown in Figure 1c. Average flow versus applied pressure is compared to Darcy's law and the equivalent channel model (Figure 6a).<sup>[39]</sup> The permeability constant ( $k$ ) is approximated using a permeability–porosity correlation (Figure 6c).<sup>[39]</sup> Values of the empirically determined

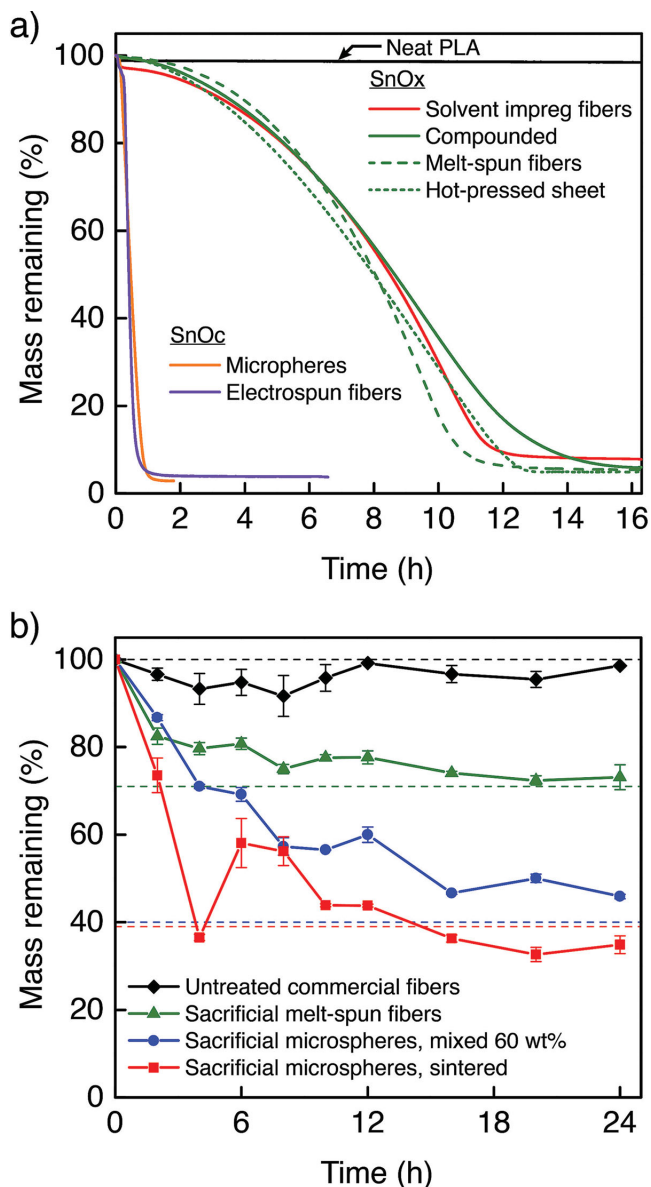


**Figure 5.** Vaporization of sacrificial components (VaSC) characterization: a) ex situ isothermal thermogravimetric analysis (iTGA, 200 °C) comparing raw sacrificial template materials (two catalyst types: tin(II) oxalate (SnOx) and tin(II) octoate (SnOc)), b) in situ mass loss of sacrificial template materials embedded in epoxy (vacuum oven, 200 °C,  $n = 4$  specimens per measurement). Error bars represent one standard deviation. Dashed lines indicate expected mass remaining (mass fraction epoxy = 1.0 – mass fraction sacrificial template) after template removal.

coefficient (0.5) and exponent of the porosity term (1.5) are taken from the literature.<sup>[40,41]</sup> The porosity is described as vesicular, with hollow spheres connected by apertures (highlighted in Figure 6b). In vesicular materials the permeability is not directly correlated to the porosity since apertures restrict flow.<sup>[40,41]</sup> Here, we use aperture area fraction in place of the porosity term ( $\phi$ ), and aperture size to determine the hydraulic radius ( $R$ ).<sup>[39–41]</sup> The area fraction and size of apertures are measured from cross-sectional scanning electron images. The measured aperture area fraction and average hydraulic radius

are used to calculate the permeability constant, which when applied to Darcy's law gives a prediction of the flow rate for a given pressure. Applying this approach yields good agreement between experimental data and model prediction.

Flow through straight, 1D channels with circular cross section is compared to the Hagen–Poiseuille equation<sup>[42]</sup> (Figure 7) with the prediction based on average channel dimensions ( $299 \pm 18 \mu\text{m}$  diameter, and  $49.8 \pm 0.5 \text{ mm}$  long). The deviation in the experimental measurements between different channels ( $\approx 24\%$ ) and the discrepancy from theory ( $\approx 13\%$ ) is believed to come from small variations in diameter due to its strong influence on flow rate ( $\propto d^4$ ).

Laser cutting to fabricate 2D network templates (Figure 3) results in trapezoidal shaped channels with rounded corners (Figure S6, Supporting Information). CAD geometries for computational fluid dynamics (CFD) simulations were generated to accurately reflect the as-fabricated geometry, with channel dimensions extracted from X-ray computed microtomographic (microCT) cross-sectional images (Figure S6, Table S3, Supporting Information). Two networks were simulated in ANSYS FLUENT: One with the upper bound of measured channel dimensions and one with the lower bound. The experimental data falls between the simulation results for these bounds as expected (Figure 8). The lower bound prediction shows closer agreement with experiments, as narrower cross-section segments would expectedly have a more pronounced influence on overall flow response due to the strong dependence on channel diameter.

Flow in the 3D specimen is compared to CFD simulation of the CAD geometry (nominal, Figure S3a, Supporting Information), which was the input for 3D printing (Figure 9). The simulated flow rate through the nominal geometry is on average 26% higher than the flow measured experimentally. Observing that the 3D-printed template is imperfect and possesses local undulations, a more precise geometric representation of channel architecture was reconstructed through microCT (Figure S3b, Supporting Information). CFD simulations based on the refined microCT geometry show closer agreement, with only 9% higher flow rate (on average) than measured experimentally.

### 3. Conclusions

In summary, we have demonstrated a technique to form multidimensional, multiscale, and interconnected vascular and porous networks in thermosetting polymers via templates of sacrificial PLA. Application of pre-existing thermal and solvent-based polymer processing techniques extends the size scale and dimensionality of templates that can be produced. The effectiveness of the VaSC process is demonstrated ex situ for raw sacrificial template materials as well as in situ when fabricated templates are embedded in an epoxy thermoset. Inverse structures created from templates of each level of dimensionality (0D–3D) are shown to have predictable flow characteristics. We aim to extend VaSC to all classes of materials, e.g., metals, ceramics, thermoplastics, etc. This extension will require development of a library of sacrificial materials with a wide range of decomposition characteristics (time, temperature, decomposition products)

**Table 1.** Specimen details for in situ VaSC characterization, embedded in epoxy. Error represents one standard deviation.

Type	Nominal dimensions [mm]			Mass% sacrificial material (# specimens)	Estimated volume% sacrificial material	Mass% lost after 24 h (# specimens)	Details
	Length	Width	Thickness				
Untreated commercial fibers (no catalyst)	50	3.5	1.1	22 ± 2 (n = 36)	19 ± 2	1.5 ± 0.3 (n = 4)	Three fibers running lengthwise (490 ± 10 μm diameter)
Sacrificial melt-spun fibers	50	3.5	1.1	29 ± 2 (n = 36)	25 ± 2	27 ± 3 (n = 4)	Three fibers running lengthwise (660 ± 50 μm diameter)
Sacrificial spheres, mixed at 60 wt% (closed cell)	15	15	0.9	60	56	54.1 ± 0.5 (n = 4)	Hand mixed into epoxy, surfaces polished after curing
Sintered sacrificial spheres (open-cell)	15	15	1	61 ± 3 (n = 5)	58 ± 3	65 ± 2 (n = 4)	Infused with epoxy via VARTM, surfaces polished after infusion and curing

while still maintaining ease of translation to conventional fabrication techniques. The VaSC platform provides a tool to reliably fabricate vascular and porous architectures across an unparalleled breadth of geometry and size scale, thus enabling vascular designs optimized by biology in modern engineering applications ranging from self-healing<sup>[24]</sup> to gas capture.<sup>[16]</sup>

#### 4. Experimental Section

**Sample Fabrication:** Unless otherwise specified, sacrificial templates were embedded in Araldite/Aradur 8605 epoxy (Huntsman Advanced Materials LLC), cured for 30 h at RT = 21 °C followed by 8 h at 121 °C, and VaSC treatment was performed at 200 °C in a vacuum oven

(≈12 Torr) for 24 h. Solvent impregnated commercial PLA fibers were produced according to the previously reported procedure.<sup>[23,24,36,37]</sup>

**0D Sacrificial Materials:** Sacrificial microspheres were manufactured using an emulsion/solvent evaporation technique. PLA pellets (2.70 g, 4 wt% with respect to solvent, Ingeo 4043D, NatureWorks LLC) and SnOc (0.135 g, 5 wt% with respect to PLA, Sigma-Aldrich) catalyst were dissolved in DCM (50 mL). The PLA solution was added to an aqueous surfactant mixture (120 mL, 1 wt% PVA, 87%–89% hydrolyzed,  $M_w = 85$ –124 kDa, Sigma-Aldrich) and mechanically stirred at 1200 rpm. Stirring was continued for 4 h at RT to allow for DCM evaporation. The suspension was centrifuged at 4000 rpm for 10 min, decanted and rinsed with deionized water. This process was repeated three times to remove the PVA. The solution was then lyophilized for 48 h, producing a free-flowing powder. To create closed-cell porous epoxy samples, sacrificial microspheres were combined with epoxy, mixed by hand, and the mixture was molded between glass plates using a silicone spacer (≈1 mm thick). For sintering to create open-cell porosity, sacrificial microspheres (≈2.4 g) were poured into an aluminum mold (49 × 49 mm<sup>2</sup>) with a fitted cover. The mold was placed in an oven at 110 °C for 4 h, with an applied pressure (≈0.5 kPa) from the weight of the cover, to produce an interconnected porous sheet (≈1 mm thick). The sheet was subsequently infiltrated with liquid epoxy using vacuum-assisted resin transfer molding (VARTM). Top and bottom surfaces were polished after curing the epoxy to expose sacrificial spheres.

**Compounding:** PLA and SnOx catalyst (Sigma-Aldrich) were melt-compounded using a twin-screw batch compounder (Plasti-corder EPL V5501 equipped with measuring head, C. W. Brabender). Catalyst was sieved to remove particles larger than 53 μm. The compounder was preheated to 170 °C. The screw rotation speed was set to 15 rpm; PLA pellets (50 g, Ingeo 4043D) were slowly added and allowed to melt while mixing. Catalyst (2.5 g SnOx) was slowly added, the chamber was closed, and mixing proceeded for 10–15 min. The melt-compounded precursor material was extracted and cut into fragments while the polymer was still warm and pliable. The sacrificial material was stored in a vacuum desiccator to prevent moisture absorption until further use.

**1D Sacrificial Materials:** Sacrificial fibers were fabricated using a lab-scale melt spinning apparatus. Melt-compounded precursor material (20 g) was dried under vacuum at 70 °C for at least 6 h. The extruder was preheated to 175 °C, after which the material was loaded into the extruder

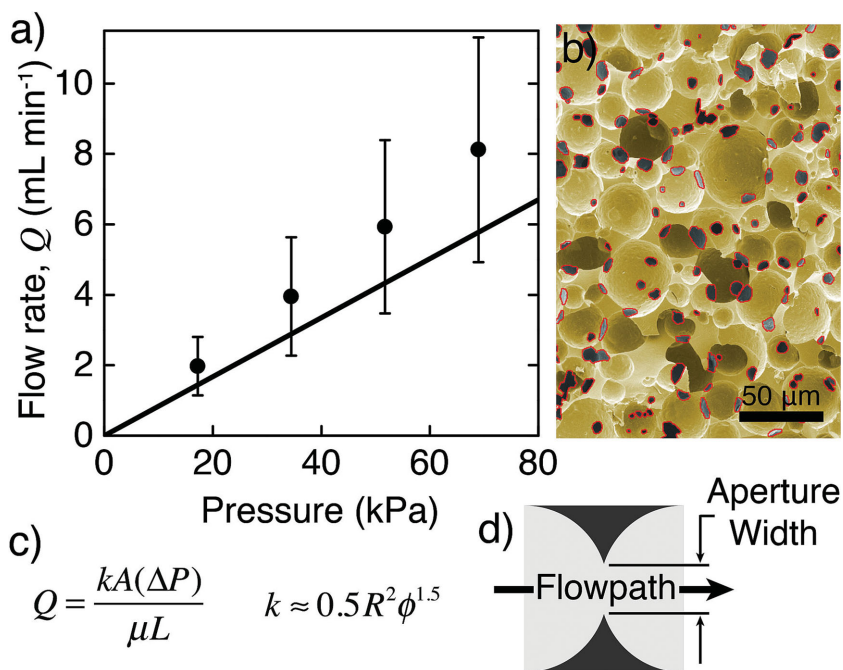


**Figure 6.** a) Flow rate evaluation of porous epoxy created from sintered sacrificial spheres (OD). Discrete points are experimental data with error bars representing one standard deviation ( $n = 3$ ), and solid line is a theoretical model based on Darcy's law and a permeability ( $k$ ) – porosity ( $\phi$ ) correlation (equations in c). b) SEM of cross-section indicating apertures (outlined in red, gold color overlay indicating nonflow area), depicted schematically in d).

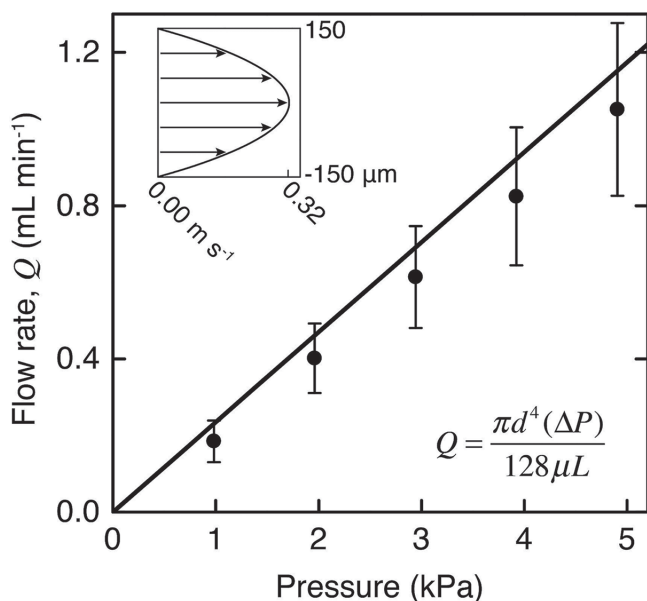


**Figure 7.** Flow rate evaluation for straight, circular channels (1D). Discrete points are experimental data with error bars representing one standard deviation ( $n = 6$ ). Solid line is theoretical model based on the Hagen–Poiseuille equation (inset, lower right). Upper left inset depicts the parabolic velocity profile characteristic of laminar flow, at input pressure of 2.9 kPa.

barrel and allowed to melt ( $\approx 45$  min). A polytetrafluoroethylene spacer and brass cylinder connected to a steel piston were inserted into the barrel and used to extrude precursor material through a 1.25 mm diameter spinneret at a rate of approximately  $5.5 \text{ g min}^{-1}$ . Fiber take-up speed was adjusted to control fiber diameter. For a fiber diameter of

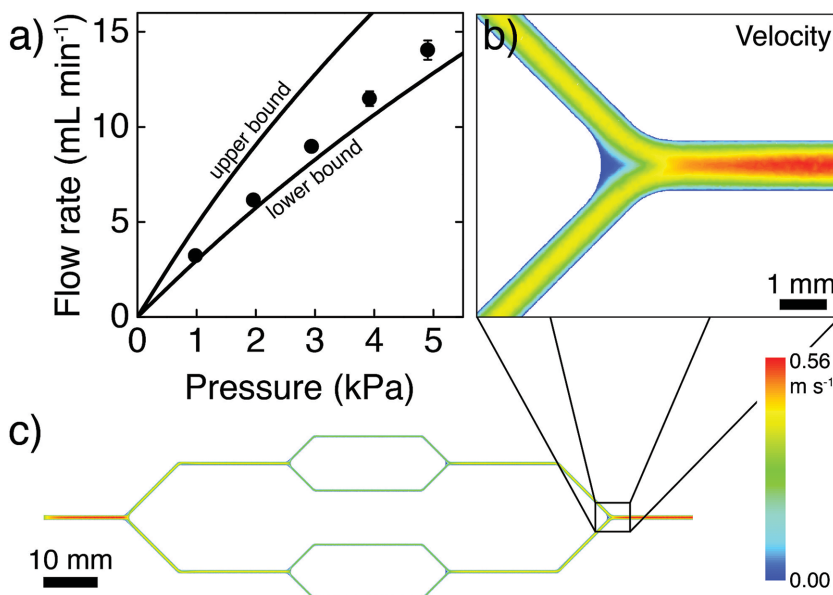


**Figure 8.** a) Flow results for bifurcating, planar network specimens (2D) shown in Figure 3. Discrete points are experimental measurements with error bars representing one standard deviation (error bars not visible are smaller than the data markers,  $n = 3$ ). Solid lines are computational fluid dynamics (CFD) simulations for lower and upper bounds based on deviation in channel dimensions. b, c) Midplane velocity profile from lower bound CFD results at 2.9 kPa input pressure.

$\approx 650 \text{ } \mu\text{m}$  (41 rpm, 88 mm take-up drum diameter), a single extrusion run produced roughly 40 m of continuous fiber. After melt spinning, sacrificial fibers were drawn to a length ratio (final/initial) of 3:1 in a heated oven ( $80 \text{ } ^\circ\text{C}$ ) by vertically suspending a weight equivalent to one-fourth the initial yield stress ( $\approx 10 \text{ MPa}$ , Figure S2, Supporting Information). The array of 1D channels embedded in epoxy in Figure 2b was cured 24 h at RT followed by 2 h at  $121 \text{ } ^\circ\text{C}$  and 3 h at  $177 \text{ } ^\circ\text{C}$ . Filament for 3D printing (FDM) ( $\approx 3 \text{ mm}$  diameter) was fabricated using the same melt spinning apparatus by extruding through a brass spinneret extension (75 mm long) with a 2.5 mm inner diameter into a RT water column. Resulting filaments of sacrificial material ranged from 2.4 to 3.1 mm diameter, within printable tolerances for the FDM equipment. Electrospun sacrificial fibers were spun from solution with a syringe pump ( $0.6 \text{ mL h}^{-1}$ , Model 780101 infusion pump, KD Scientific) using a blunt tip dispensing needle (outer diameter 0.72 mm and inner diameter 0.41 mm) and 15 kV DC power supply (Model RHR30PN10, Spellman) applied across a gap of 15 cm. PLA powder (2.5 g, 25 wt% with respect to solvent, Ecorene NW40, ICO polymers) and SnO<sub>c</sub> (0.125 g, 5 wt% with respect to PLA) were dissolved in solvent (7.5 g, 3:1 by volume chloroform/acetone). Sacrificial fibers were spun onto a copper parallel plate collector with 3 cm gap distance, embedded in epoxy (EPON 828/EPIKURE 3300, Momentive) and cured 24 h at RT followed by 90 min at  $82 \text{ } ^\circ\text{C}$  and 90 min at  $121 \text{ } ^\circ\text{C}$ . To expose channels after VaSC, specimens were freeze fractured after submersion in liquid N<sub>2</sub>.

**2D Sacrificial Materials:** Sheets of sacrificial material were fabricated using a hot press (Model 14, Tetrahedron). Melt-compounded precursor material (10 g) was placed between two aluminum plates with a 500  $\mu\text{m}$  spacer. A compressive force of 2.22 kN was applied while temperature was ramped to  $177 \text{ } ^\circ\text{C}$  ( $10 \text{ } ^\circ\text{C min}^{-1}$ ). After heating, the force was increased to 89 kN and held for 10 min. The temperature was ramped down to RT ( $10 \text{ } ^\circ\text{C min}^{-1}$ ) after which the load was removed. The resulting sheet was laser cut (Pro LF Series  $48 \times 36 \text{ in.}^2$  CO<sub>2</sub> laser, 90 W, Full Spectrum Laser LLC) with a power of 5% and speed of 100%. The width of the laser cut is approximately 120  $\mu\text{m}$ , which was accommodated by oversizing the CAD pattern 60  $\mu\text{m}$  on all sides.

**3D Sacrificial Materials:** Freestanding sacrificial templates were printed using a desktop FDM (AO-100, Lulzbot). A solid model of the geometry was created via CAD (SolidWorks v.2011, Dassault Systèmes) and converted to stereolithography (STL) data format. The STL file was then converted to printable G-code using open source software (Slic3r v0.9.10b). The print file was sliced into 322 layers, which took approximately 1 h to print with a 75% infill. Printing was conducted with a nozzle diameter of 0.35 mm, a nozzle temperature of  $180 \text{ } ^\circ\text{C}$ , and a bed temperature of  $82 \text{ } ^\circ\text{C}$ . The printer bed was covered with polyethylene terephthalate tape and roughened with light sanding to enhance surface adhesion of the printed material. The printed structure was painted with a solution of PLA and SnO<sub>x</sub> catalyst before epoxy infusion producing a solid layer of PLA on the outer walls of the sacrificial template, thereby preventing epoxy from infiltrating the otherwise porous structure. The embedded 3D template underwent VaSC treatment for 48 h at  $200 \text{ } ^\circ\text{C}$ .

**Imaging:** Microsphere dimensions were determined using optical images (DMR optical microscope, Leica; Micropublisher 3.3 CCD, QImaging) and ImageJ (National Institute of Health) image processing software. Porosity of epoxy structures was analyzed using scanning electron microscopy (SEM) images (XL30 ESEM-FEG, Philips). ImageJ software was used to highlight apertures or pores, and determine size and area fraction. MicroCT of was performed

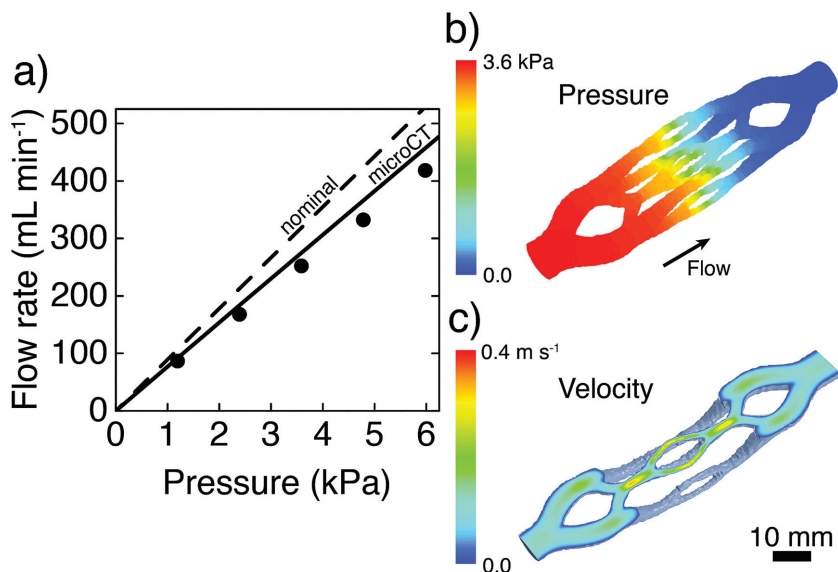


**Figure 9.** a) Flow results for printed tree-like structure (3D) ( $n = 1$ ). Discrete points are experimental data, error bars representing one standard deviation from three measurements on the same specimen are smaller than the data markers. CFD models of nominal (dashed line) and microCT (solid line) geometries. b) Pressure and c) velocity (midplane cross section) profiles from CFD of microCT at 3.6 kPa input pressure.

on an Xradia BioCT (MicroXCT-400). 2D and 3D specimens were filled with a radiocontrast agent (Omnipaque 350, GE Healthcare). Additional microCT scan settings are included in Table S1 (Supporting Information). Data were reconstructed using TXM Reconstructor (v.8.1, Xradia) and visualized in 3D with TXM3Dviewer (v.1.1.6, Xradia). MicroCT images of the open-cell porous epoxy structure (0D) were reproduced in Amira (v.5.5.0, FEI) to isolate the matrix material, determine the porosity volume fraction, and create videos and still images. 1D specimens made from electrospun fibers were filled with a fluorescent dye (0.03 wt% Rhodamine in deionized water) via vacuum infiltration. Filled channels were imaged using confocal fluorescence microscopy (TCS SP2, Leica) with the following acquisition parameters: excitation wavelength: 543 nm; emission wavelengths: 562–617 nm; objective: 63.0 $\times$ , 1.4 NA, oil immersion lens; confocal pinhole diameter: 115  $\mu\text{m}$ ; voxel size: 0.116  $\mu\text{m} \times 0.116 \mu\text{m} \times 0.122 \mu\text{m}$ . Confocal images were reconstructed in Amira.

**Isothermal Thermogravimetric Analysis (iTGA):** iTGA was performed on a Mettler-Toledo TGA851e, calibrated with indium, aluminum, and zinc standards. For each experiment, the sample ( $\approx 8$  mg) was weighed into an alumina crucible. The mass loss was recorded during an isothermal hold at 200  $^{\circ}\text{C}$  for up to 16 h, with a ramp rate of 20  $^{\circ}\text{C min}^{-1}$  from 25  $^{\circ}\text{C}$  under continuous nitrogen purge.

**In Situ VaSC Characterization:** In situ mass loss evaluation was performed in a vacuum oven set to 200  $^{\circ}\text{C}$  under  $\approx 12$  Torr (abs) vacuum, the conditions for VaSC.<sup>[23,24,36,37]</sup> The mass of sacrificial material lost, i.e., converted to gaseous lactide monomer, was measured as a function of time (Figure 5b). Four specimens were tested for each combination of specimen type (Table 1) and treatment time (2, 4, 6, 8, 10, 12, 15, 18, 21, 24 h). Each treatment time was evaluated separately (to limit uncontrolled heating and cooling from opening and closing the oven door) as follows: specimens for one treatment time were placed in the preheated vacuum oven, the oven door was sealed, and vacuum was started immediately. The time increment began once the specimens were placed in the vacuum oven. The mass of each specimen was measured prior to and following thermal treatment. The melt-spun fiber specimens were sandwiched between two aluminum plates (to evenly distribute heat), and absorbent bleeder cloth. The porous sphere type specimens were not sandwiched between plates and bleeder cloths since doing so would obstruct the two largest surfaces of the specimens, and hinder escape of gaseous depolymerization products.

**Flow Testing:** Pressure was applied using either a static pressure head (1D, 2D, 3D) or computer controlled (LabVIEW v.2013, National Instruments) pressure pump (0D) (Ultimus V, Nordson EFD) at RT = 21  $^{\circ}\text{C}$ . The test liquid was deionized water (0D, 1D, 2D) or 85/15 wt% glycerol/water mixture (3D) (103 cP,<sup>[43]</sup> measured on a TA instruments AR-G2 rheometer using a double gap concentric cylinder geometry at 21  $^{\circ}\text{C}$ ). Mass flow rate data was collected at 10 Hz using a computer-interfaced analytical balance (XS204 DeltaRange, Mettler Toledo). Experiments were performed under laminar flow conditions (Table S4, Supporting Information) and compared to appropriate predictive models.

**Darcy's Law and the Equivalent Channel Model:** The flow through porous media is described by Darcy's Law:<sup>[39]</sup>

$$Q = \frac{kA(\Delta P)}{\mu L} \quad (1)$$

in which volumetric flow rate ( $Q$ ) is proportional to the pressure gradient ( $\Delta P$ ), permeability constant ( $k$ ), and the cross-sectional area ( $A$ ), while being inversely proportional to the dynamic viscosity ( $\mu$ ) and length ( $L$ ). The permeability constant ( $k$ ) can be measured, but it is also useful to have a method for calculating based on geometry. Permeability is related to the porosity of the material as

well as pore microstructure (pore shape, connectivity, and pathway tortuosity).<sup>[39–41]</sup> The equivalent channel model assumes that pores can be approximated by a set of channels running through the material. Under this assumption the permeability ( $k$ ) can be related to porosity ( $\phi$ ) by:<sup>[39]</sup>

$$k \approx CR^2\phi^m \quad (2)$$

where the shape factor ( $C$ ) and exponent ( $m$ ) are empirically determined parameters, the hydraulic radius ( $R$ ) is the dimension describing the flow cross-section, and porosity ( $\phi$ ) is measured. The shape factor ( $C$ ) describes the shape of the flow cross section, and has values from 1/2 to 1/3 for circular to slit-like geometries, respectively. The exponent ( $m$ ) has values from 1 to 3, with 1 representing the case of a straight channel. The porous epoxies here have a similar microstructure to scoria vesicular basalts considered by Saar et al.<sup>[40,41]</sup> Based on these works, a value of  $m = 1.5$  was used, which is appropriate for perfectly spherical voids. In Saar's works, the prediction of permeability was from porosity and was  $\approx 10^4$  times larger than measured the permeability. However, it was reported that flow is primarily governed by the narrow opening (apertures) that are  $\approx 10$  times smaller than the diameter of the overlapping spheres. Here, we analyzed images ( $n = 2$ ) of the cross section and isolated the apertures (Figure 3b). The aperture area fraction (6.96%) was used in place of the porosity term ( $\phi$ ) in Equation (2). The diameter of each aperture ( $d$ ) was determined using its area ( $A$ ), assuming circular shape so that  $A = \pi d^2/4$ . The average hydraulic radius ( $R$ ) was calculated as one quarter of the average aperture diameter ( $d_{\text{average}} = 5.97 \mu\text{m}$ ).<sup>[37]</sup> A shape factor ( $C$ ) of 1/2 was used since the apertures are approximately circular. The permeability was calculated using Equation (2), which was in turn used to predict flow rate using Equation (1). These predicted results are compared to experimentally measured flow rates in the plot shown in Figure 6.

**Computational Fluid Dynamics (CFD) Simulation:** Finite volume CFD simulations (FLUENT v.15.0, ANSYS) were performed on 2D and 3D models using CAD (SolidWorks) and reconstructed microCT geometries meshed in ANSYS Meshing. Navier–Stokes equations were solved using the SIMPLE pressure–velocity scheme, Green–Gauss node-based gradient discretization, second-order pressure discretization, and

third-order MUSCL momentum discretization. Numerical convergence was defined as when continuity and velocity residuals fell below  $10^{-6}$ . The pressure-inlet boundary condition was used to drive flow; at least five inlet pressures were simulated per model to generate flow rate versus pressure curves. For the 2D bifurcating channel network, CAD geometries were generated with trapezoidal channels based on measured dimensions (Figure S6, Table S3, Supporting Information). Two models were simulated: one with the lower bounds of measured dimensions and one with the upper bounds. To confirm mesh independence of the simulations, the flow rate of water through the lower bound model at an applied pressure of 2.94 kPa was tracked at different mesh sizes (Figure S9, Supporting Information). A final volumetric mesh consisting of 1.10 million tetrahedral elements was chosen, such that there were a sufficient number of elements to be within 1% of the converged flow rate. The same mesh element sizing was used to mesh the higher bound model; the resulting volumetric mesh consisted of 1.49 million tetrahedral elements. The nominal CAD geometry (the input for 3D printing) of the 3D tree-like structure was used to generate a mesh for simulation. Symmetry was used such that only half of the network needed to be modeled. Mesh independence was confirmed by tracking the flow rate of 85/15 wt% glycerol/water through the network at an applied pressure of 3.59 kPa (Figure S10, Supporting Information). A final volumetric mesh consisting of 0.56 million tetrahedral elements was chosen, such that there were a sufficient number of elements to be within 1% of the converged flow rate. MicroCT data was used to construct a more accurate model for simulation of the 3D structure. Amira was used to segment (isolate) the entire vascular structure and generate a triangular surface mesh consisting of 0.4 million elements. A nonuniform rational B-spline (NURBS) surface was generated from the surface mesh using Geomagic Studio (v.2014.1.0, 3D Systems). SolidWorks was employed to translate the NURBS surface into a solid model (Figure S3b, Supporting Information). The solid model was used to generate volume meshes of different sizes and mesh refinement was tracked in the same manner as the nominal model (Figure S11, Supporting Information). A final volumetric mesh consisting of 14.4 million tetrahedral elements was chosen. Note that the coarsest mesh (8.3 million elements) did not fully converge to  $10^{-6}$  residual tolerances, as it was not fine enough to capture the high level of surface detail from the microCT scan.

## Supporting Information

Supporting Information is available from the Wiley Online Library or from the author.

## Acknowledgements

This work has been financially supported by the Air Force Office of Scientific Research (AFOSR, grant numbers FA9550-10-1-0255, FA9550-09-1-0686), and the Center for Electrical Energy Storage, an Energy Frontier Research Center funded by the U.S. DOE, the Office of Basic Energy Sciences (grant number 615 DOE ANL 9F-31921). S.J.P. is supported by the Department of Defense (DoD), AFOSR, the National Defense Science and Engineering Graduate (NDSEG) Fellowship, 32 CFR 168a. T.D. is supported under contract FA9550-11-C-0028, awarded by the DoD, AFOSR, NDSEG Fellowship, 32 CFR 168a. A.M.C. is supported by the National Science Foundation Graduate Research Fellowship under grant number DGE 11-44245. The authors extend our gratitude to the Beckman Institute for facilities, Leilei Yin for assistance with microCT, Travis Ross for assistance with Geomagic, and S. Tsubaki-Liu and Y. Fedonina, for assistance with sample fabrication and testing. They acknowledge Hefei Dong for helpful discussions during early development of the work.

Received: October 20, 2014  
Revised: November 19, 2014  
Published online:

- [1] N. A. Campbell, J. B. Reece, *Biology*, Benjamin-Cummings Publishing Company, San Francisco, CA, USA **2002**.
- [2] M. A. Unger, H. P. Chou, T. Thorsen, A. Scherer, S. R. Quake, *Science* **2000**, *288*, 113.
- [3] J. R. Anderson, D. T. Chiu, R. J. Jackman, O. Cherniavskaya, J. C. McDonald, H. Wu, S. H. Whitesides, G. M. Whitesides, *Anal. Chem.* **2000**, *72*, 3158.
- [4] L. M. Bellan, S. P. Singh, P. W. Henderson, T. J. Porri, H. G. Craighead, J. A. Spector, *Soft Matter* **2009**, *5*, 1354.
- [5] J. Lee, J. Paek, J. Kim, *Lab Chip* **2012**, *12*, 2638.
- [6] S. M. Berry, T. J. Roussel, S. D. Cambron, R. W. Cohn, R. S. Keynton, *Microfluid. Nanofluid.* **2012**, *13*, 451.
- [7] C. K. Harnett, G. W. Coates, H. G. Craighead, *JVST B* **2001**, *19*, 2842.
- [8] S. Park, Y. S. Huh, K. Szeto, D. J. Joe, J. Kameoka, G. W. Coates, J. B. Edel, D. Erickson, H. G. Craighead, *Small* **2010**, *6*, 2420.
- [9] B. Dang, M. S. Bakir, D. C. Sekar, C. R. King, J. D. Meindl, *IEEE Trans. Adv. Packag.* **2010**, *33*, 79.
- [10] D. Bhusari, H. A. Reed, M. Wedlake, A. M. Padovani, S. A. Bidstrup-Allen, P. A. Kohl, *J. Microelectromech. Syst.* **2001**, *10*, 400.
- [11] P. A. Kohl, Q. Zhao, K. Patel, D. Schmidt, S. A. Bidstrup-Allen, R. Shick, S. Jayaraman, *Electrochem. Solid-State Lett.* **1998**, *1*, 49.
- [12] H. A. Reed, C. E. White, V. Rao, S. A. Bidstrup-Allen, C. L. Henderson, P. A. Kohl, *J. Microelectromech. Syst.* **2001**, *11*, 733.
- [13] J. P. Jayachandran, H. A. Reed, H. Zhen, L. F. Rhodes, C. L. Henderson, S. A. Bidstrup-Allen, P. A. Kohl, *J. Microelectromech. Syst.* **2003**, *12*, 147.
- [14] H. Suh, P. Bharathi, D. J. Beebe, J. S. Moore, *J. Microelectromech. Syst.* **2000**, *9*, 198.
- [15] L. S. Loo, K. K. Gleason, *Electrochem. Solid-State Lett.* **2001**, *4*, G81.
- [16] D. T. Nguyen, Y. T. Leho, A. P. Esser-Kahn, *Lab Chip* **2012**, *12*, 1246.
- [17] J. A. Potkay, M. Magnetta, A. Vinson, B. Cmolik, *Lab Chip* **2011**, *11*, 2901.
- [18] A. Z. Weber, M. M. Mench, J. P. Meyers, P. N. Ross, J. T. Gostick, Q. Liu, *J. Appl. Electrochem.* **2011**, *41*, 1137.
- [19] X. Li, I. Sabir, *Int. J. Hydrogen Energy* **2005**, *30*, 359.
- [20] B. K. Paul, P. Kwon, R. Subramanian, *J. Manuf. Sci. Eng.* **2006**, *128*, 977.
- [21] K. J. Maloney, K. D. Fink, T. A. Schaedler, J. A. Kolodziejka, A. J. Jacobsen, C. S. Roper, *Int. J. Heat Mass Transfer* **2012**, *55*, 2486.
- [22] K. S. Toohy, N. R. Sottos, J. A. Lewis, J. S. Moore, S. R. White, *Nat. Mater.* **2007**, *6*, 581.
- [23] A. P. Esser-Kahn, P. R. Thakre, H. Dong, J. F. Patrick, V. K. Vlasov, N. R. Sottos, J. S. Moore, S. R. White, *Adv. Mater.* **2011**, *23*, 3654.
- [24] J. F. Patrick, K. R. Hart, B. P. Krull, C. E. Diesendruck, J. S. Moore, S. R. White, N. R. Sottos, *Adv. Mater.* **2014**, *26*, 4302.
- [25] B. Van der Bruggen, C. Vandecasteele, T. Van Gestel, W. Doyen, R. Leysen, *Environ. Prog.* **2003**, *22*, 46.
- [26] H. Zhang, X. Yu, P. V. Braun, *Nat. Nanotechnol.* **2011**, *6*, 277.
- [27] P. Arora, Z. Zhang, *Chem. Rev.* **2004**, *104*, 4419.
- [28] D. W. Huttmacher, *Biomaterials* **2000**, *21*, 2529.
- [29] R. A. Barry, R. F. Shepherd, J. N. Hanson, R. G. Nuzzo, P. Wiltzius, J. A. Lewis, *Adv. Mater.* **2009**, *21*, 2407.
- [30] J. S. Miller, K. R. Stevens, M. T. Yang, B. M. Baker, D. T. Nguyen, D. M. Cohen, E. Toro, A. A. Chen, P. A. Galie, X. Yu, R. Chaturvedi, S. N. Bhatia, C. S. Chen, *Nat. Mater.* **2012**, *11*, 768.
- [31] T. Jiang, W. I. Abdel-Fattah, C. T. Laurencin, *Biomaterials* **2006**, *27*, 4894.
- [32] L. J. Gibson, M. F. Ashby, B. A. Harley, *Cellular Materials in Nature and Medicine*, Cambridge University Press, Cambridge, UK **2010**.
- [33] J. Huang, J. Kim, N. Agrawal, A. P. Sudarsan, J. E. Maxam, A. Jayaraman, V. M. Ugaz, *Adv. Mater.* **2009**, *21*, 3567.
- [34] D. Theriault, S. R. White, J. A. Lewis, *Nat. Mater.* **2003**, *2*, 265.

- [35] C. Gualandi, A. Zucchelli, M. F. Osorio, J. Belcari, M. L. Focarete, *Nano Lett.* **2013**, *13*, 5385.
- [36] H. Dong, A. P. Esser-Kahn, P. R. Thakre, J. F. Patrick, N. R. Sottos, S. R. White, J. S. Moore, *ACS Appl. Mater. Interfaces* **2012**, *4*, 503.
- [37] A. M. Coppola, P. R. Thakre, N. R. Sottos, S. R. White, *Composites, Part A* **2014**, *59*, 9.
- [38] Z. Huang, Y. Zhang, M. Kotaki, S. Ramakrishna, *Compos. Sci. Technol.* **2003**, *63*, 2223.
- [39] M. S. Paterson, *Mech. Mater.* **1983**, *2*, 345.
- [40] M. O. Saar, M. Manga, *Geophys. Res. Lett.* **1999**, *26*, 111.
- [41] M. O. Saar, *Master's Thesis*, University of Oregon, **1998**.
- [42] Y. A. Çengel, R. H. Turner, *Fundamentals of Thermal-Fluid Sciences* McGraw-Hill Higher Education, New York, NY, USA **2001**.
- [43] J. B. Segur, H. E. Oberstar, *Ind. Eng. Chem.* **1951**, *43*, 2117.
-